Ultrahigh thermoelectric performance in RbGeI$_3$/CsSnI$_3$ superlattices

Yaorong Luo [1], Xu Li [1], Hao Cheng [1], Bingxuan An,[1] Lan Chen,[1,2] Jian Zhou,[1] Di Wu,[1,*] and Yurong Yang[1,†]

[1]*Department of Materials Science and Engineering, National Laboratory of Solid State Microstructures and Collaborative Innovation Center of Advanced Microstructures, Jiangsu Key Laboratory of Artificial Functional Materials, Nanjing University, Nanjing 210093, China*
[2]*School of Science, Nanjing University of Posts and Telecommunications, Nanjing 210023, China*

By first-principles methods combined with Boltzmann transport theory, we perform a systematic investigation of the thermoelectric properties of RbGeI$_3$/CsSnI$_3$ superlattices. RbGeI$_3$/CsSnI$_3$ superlattices construct a quantum well with valence and conduction states near the Fermi level located in CsSnI$_3$ layers, which yields a periodic repetition of two-dimensional transport channels. The quantum-confinement effects and the ultralow lattice thermal conductivity of the superlattices greatly enhance the in-plane thermoelectric power factor and figure of merit (ZT), which further increase when decreasing the thickness of CsSnI$_3$ layers in the superlattices. In (RbGeI$_3$)$_5$/(CsSnI$_3$)$_1$ superlattice, the power factor increases by two times, and ZT is enhanced by nine times, compared to the parent CsSnI$_3$. The ZT of this superlattice is 1.34 at 300 K and 3.78 at 550 K, providing a potential candidate for room-temperature thermoelectric applications. These results also confirm a way to improve the thermoelectric performance of CsSnI$_3$.

I. INTRODUCTION

Thermoelectric (TE) materials that can generate a direct and reversible conversion between heat and electricity without any moving parts have attracted increasing attention as a promising clean-energy technology [1–4]. The performance of a TE material is largely determined by the dimensionless figure of merit $ZT = S^2 \sigma T / (\kappa_{ele} + \kappa_L)$, where S, σ, T, κ_{ele}, and κ_L represent the Seebeck coefficient, electrical conductivity, temperature, electronic thermal conductivity, and lattice thermal conductivity, respectively. It is clear that a greater ZT may be achieved by either raising the numerator ($S^2\sigma$) and/or lowering the denominator (κ_{ele} and κ_L) based on the preceding formula. However, the strong coupling effect among S, σ, and κ_{ele} usually impedes the improvement of TE performance. Proven strategies for improving ZT are typified either by an enhancement of power factor ($S^2\sigma$) via band engineering approaches [4–6] or by a suppression of the only relatively independent material property, lattice thermal conductivity (κ_L) through phonon scattering due to various sources [7,8]. The decoupling studies of electron and phonon transports reveal that the semiconductor material with intrinsic ultralow lattice thermal conductivity is very promising as a high-performance TE material.

Halide perovskite materials of ABX_3 (X = F, Cl, Br, I) not only show broadly anticipated applications in photovoltaic and light-emitting devices due to their extraordinary optoelectronic properties [9] but also hold great promise for TE applications, as they may offer ultralow thermal conductivities [10] and large charge mobilities [11–13]. In 2014, He and Galli [14] first investigated the TE properties of CH$_3$NH$_3$MI$_3$ (M = Pb, Sn) by using first-principles density functional theory calculations and found that the predicted ZT can reach values ranging from 1 to 2 after assuming the lattice thermal conductivity of 1 W m^{-1} K^{-1}. Shortly afterwards, on the experimental front, Mettan *et al.* [15] also studied the CH$_3$NH$_3$MI$_3$ (M = Pb, Sn) bulk crystals and found that the ZT can be improved by photoinduced doping (in CH$_3$NH$_3$PbI$_3$) and chemical doping (in CH$_3$NH$_3$SnI$_3$). In addition to the above hybrid organic-inorganic halide perovskites, the TE properties of all-inorganic halide perovskites have attracted considerable attention [16–18], especially for tin-based halide perovskites [19–21], owing to the considerable amount of intrinsic tin vacancies and the self-doping process through the oxidation of Sn^{2+} to Sn^{4+} [19,22]. Lee *et al.* [21] investigated a series of single-crystalline all-inorganic halide perovskites (CsPbBr$_3$, CsPbI$_3$, and CsSnI$_3$) and revealed that the CsSnI$_3$ possesses a ZT of 0.11 at 320 K, which is attributable to the rare combination of ultralow thermal conductivity (0.38 ± 0.04 W m^{-1} K^{-1}), high electrical conductivity (282 S cm^{-1}), and high hole mobility (394 cm^2 V^{-1} s^{-1}). Recent studies for TE properties of tin-based halide perovskites focus on the mixed perovskite containing A-site [23], B-site [24], and X-site [19,20] alloying. Liu *et al.* [20] reported that CsSnI$_{3-x}$Cl$_x$ films obtained from thermal evaporation methods can achieve a ZT of 0.14 ± 0.01 at 345 K for x = 1%. Although the TE properties of tin-based halide perovskites have been improved, the experimental ZT values observed at room temperature rarely exceed 0.2 [25,26], as shown in Supplemental Material Table S1 [27] (see also Refs. [19–21,23,24,28–34] therein). Therefore, the ZT of tin-based halide perovskites may be further improved by appropriate strategies.

One promising avenue to improve TE properties is the quantum-well superlattice, proposed by Hicks and Dresselhaus [30], which could enable both the suppression of

*diwu@nju.edu.cn
†yangyr@nju.edu.cn

085305-1

thermal conductivity and the increase of the power factor. In a quantum-well superlattice, the electrons and/or holes are quantum confined to move within the narrow-band-gap semiconductor, which has been confirmed experimentally with the use of the $PbTe/Pb_{0.927}Eu_{0.073}Te$ multiple quantum well (MQW) [35,36]. In 2007, a break-through experiment [37] reported a record $ZT \sim 2.4$ for the MQW composed of $SrTiO_3$ (barrier)/$SrTi_{0.8}Nb_{0.2}O_3$ (well)/$SrTiO_3$ (barrier) having the two-dimensional electron gas as the active region. For similar materials and structures, Choi *et al.* [38] observed a threefold enhancement of the polaron effective mass and relaxation time when the $Nb:SrTiO_3$ layer thickness is reduced from 11 to 1 unit cell. The role of quantum confinement and/or superlattice engineering to enhance and design TE has been assessed in abundant perovskite oxides, such as $LaNiO_3/LaAlO_3$ [39,40], $LaNiO_3/SrTiO_3$ [41], $SrRuO_3/SrTiO_3$ [42], $LaAlO_3/SrTiO_3$ [43,44], and $SrXO_3/SrTiO_3$ (X = V, Cr, or Mn) superlattices [45,46]. However, systematic studies on the TE properties of $CsSnI_3$-based superlattices are still lacking because of the difficulty in finding an appropriate barrier material for $CsSnI_3$ quantum wells in preparing the quantum-well superlattices [31,36].

Here, we studied the thermoelectric properties of $RbGeI_3/CsSnI_3$ superlattices by first principles combined with Boltzmann transport theory. $RbGeI_3/CsSnI_3$ is a quantum-well superlattice where the band offset is large between $CsSnI_3$ and $RbGeI_3$ [47]. In the $RbGeI_3/CsSnI_3$ superlattices, we observe the two-dimensional conduction channels ($Sn-I_2$ atomic layer) which are derived from the band offset in the valence band edge. Meanwhile, the improvement in in-plane power factor and ZT is achieved for $RbGeI_3/CsSnI_3$ superlattices due to the two-dimensional quantum-confinement effects and the ultralow lattice thermal conductivity. The ZT of $RbGeI_3/CsSnI_3$ superlattices can be as large as 1.34 (3.78) at 300 K (550 K), nine times larger than that of $CsSnI_3$ pure structure.

II. COMPUTATIONAL METHODS

The first-principles calculations were performed by the Vienna *ab initio* simulation package (VASP) code [48,49] based on density functional theory. We use the generalized gradient approximations (GGAs) with the Perdew-Burke-Ernzerhof revised for solids (PBEsol) [50] exchange-correlation functional, which has been proved to yield more accurate lattice constants and phonon frequencies than other GGA functionals [51]. The valence electron configurations of the atoms are Cs ($5s^2 4p^6 6s^1$), Rb ($4s^2 4p^6 5s^1$), Sn ($4s^2 4p^2$), Ge ($4s^2 4p^2$), and I ($5s^2 5p^5$). A plane wave energy cutoff of 350 eV and a convergence criterion of 10^{-7} eV were utilized in the electronic self-consistent calculations. The energy cutoff convergence test has been considered, as shown in Supplemental Material Fig. S1 [27]. During the structural relaxation, crystal structures including the internal positions were optimized until atomic forces were smaller than 5 meV/Å. A Monkhorst-Pack k-point mesh of $8 \times 8 \times 6$ was applied for relaxing structures and calculating electronic properties.

The phonon calculations were carried out by the PHONOPY [52] code. The lattice thermal conductivity, phonon lifetime, and phonon group velocity were carried out by the PHONO3PY

[53] code with the finite displacement method. The sixth nearest neighbor (5 Å) was chosen as the three-atom interactions cutoff distance for the third-order interatomic force constants (IFCs). For the case of $RbGeI_3$ and $CsSnI_3$, we use a $2 \times 2 \times 2$ supercell (160 atoms) and a $2 \times 2 \times 1$ supercell (80 atoms) of the unit cell for calculating the second-order and third-order IFCs, respectively. For the case of $(RbGeI_3)_m/(CsSnI_3)_n$ (m = 1, 2, 3, 4, 5; n = 5, 4, 3, 2, 1; $m + n = 6$) superlattices, we use a $2 \times 2 \times 1$ supercell (240 atoms) and a $1 \times 1 \times 1$ supercell (60 atoms) of the unit cell for calculating the second-order and third-order IFCs, respectively. Calculating the third-order IFCs requires a significantly larger number of displaced supercell structures. We note that the number of third-order IFC calculations are 12924, 13284, 13644, 13788, and 13716 for $(RbGeI_3)_m/(CsSnI_3)_n$ superlattices (SLs; from 1/5 SL to 5/1 SL), respectively. Note that the order of the magnitude of the number has been confirmed to be sufficient to obtain accurate lattice thermal conductivity [54,55]. Nonanalytical term correction [56] was applied to the IFCs to take into account the long-range Coulomb forces effects. Converged lattice thermal conductivity results were obtained by using a q mesh of $16 \times 16 \times 16$ (see Fig. S2 in the Supplemental Material [27] for the convergence test).

The electronic transport coefficients were calculated by the linearized Boltzmann transport equation within the relaxation-time approximation as implemented in the second version of the BOLTZTRAP (BOLTZTRAP2) [28] code. A dense k-point mesh with a Kmesh-resolved value of 0.05 Å^{-1} was used in the calculation of transport coefficients. An interpolation factor of 100 was used during the BOLTZTRAP2 routine.

III. RESULTS AND DISCUSSION

A. Structure and stability

Both $CsSnI_3$ and $RbGeI_3$ are orthorhombic perovskite structures with an antiferrodistortive tilting pattern of $a^-a^-c^+$ (Glazer's notation [57]). $CsSnI_3$ and $RbGeI_3$ possess the $Pnma$ (#62) and $Pna2_1$ (#33) phases, respectively, as shown in Figs. 1(a) and 1(b). It is noted that the $Pna2_1$ phase of $RbGeI_3$ is a polar structure with a 9.83 $\mu C/cm^2$ polarization along the [001] direction from our previous studies [47]. The calculated lattice parameters of $CsSnI_3$ (a = 8.77 Å, b = 8.40 Å, and c = 12.24 Å) and $RbGeI_3$ (a = 8.33 Å, b = 8.03 Å, and c = 11.68 Å) are well consistent with experiments [21,22,47]. The angles of in-plane out-of-phase (out-of-plane in-phase) octahedral tilting are 6.84 ° (10.81 °) and 7.34 ° (10.97 °) for $CsSnI_3$ and $RbGeI_3$, respectively. The calculated phonon dispersions and phonon density of states (DOS) of $CsSnI_3$ and $RbGeI_3$ are depicted in Supplemental Material Fig. S3 [27]. The absence of imaginary eigenvalues corroborates the dynamic stability and indicates that reliable lattice thermal conductivity can be obtained. Superlattices $(RbGeI_3)_m/(CsSnI_3)_n$ (m = 1, 2, 3, 4, 5; n = 5, 4, 3, 2, 1; $m + n = 6$) are considered, for which an m unit layer of $RbGeI_3$ successively alternated with an n unit layer of $CsSnI_3$ along the pseudocubic [001] direction. Figure 1(c) shows the representative configurations of the $(RbGeI_3)_5/(CsSnI_3)_1$ superlattice. The superlattices adopt a monoclinic phase (space group Pc, No. 7) with a similar antiferrodistortive tilting pattern of $a^-a^-c^+$ as their parent structures of $CsSnI_3$ and
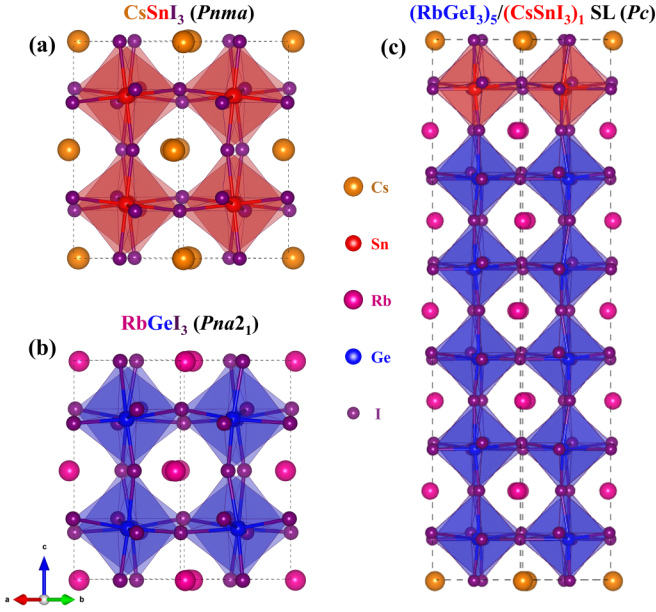
FIG. 1. Atomic structures. The structures of (a) $CsSnI_3$, (b) $RbGeI_3$, and (c) $(RbGeI_3)_5/(CsSnI_3)_1$ superlattice (5/1 SL). Orange, red, magenta, blue, and purple balls represent the Cs, Sn, Rb, Ge, and I atoms, respectively.

$RbGeI_3$. Furthermore, the superlattices display both in-plane and out-of-plane polarization, resulting from the unequal displacements of different A-site and B-site atoms [58].

B. Ultralow lattice thermal conductivity

The lattice thermal conductivity (κ_L) is calculated by solving the linearized phonon Boltzmann transport equation with the single-mode relaxation-time (SMRT) method in PHONO3PY as below [53]:

$$\kappa_L = \frac{1}{NV_0} \sum_{\lambda} C_\lambda v_\lambda^2 \tau_\lambda^{SMRT}, \qquad (1)$$

where N is the number of unit cells in the crystal and V_0 is the volume of a unit cell; C_λ, v_λ, and τ_λ^{SMRT} are the mode-specific heat capacity, phonon group velocity, and phonon lifetime, respectively, for the λth phonon mode. We calculate the frequency-dependent phonon group velocities and phonon lifetimes of $CsSnI_3$ and $RbGeI_3$, as illustrated in Fig. 2. The insets of Fig. 2 are the average phonon group velocities along the a, b, and c axes and the average phonon lifetime. As shown in Figs. 2(a) and 2(c), $RbGeI_3$ possesses lower average phonon group velocities than $CsSnI_3$, but the distribution of square of phonon group velocities of $CsSnI_3$ and $RbGeI_3$ are very similar. In the low-mid-frequency region, they all possess high-density phonon modes with low group velocities. In the mid-high-frequency region, they own low-density phonon modes with slightly higher group velocities. Figures 2(b) and 2(d) reveal the different distribution ranges of phonon lifetime for $CsSnI_3$ and $RbGeI_3$. Most phonon lifetimes of $CsSnI_3$ are within the range of 0.5–3 ps and it is between 0.3 and 1.0 ps for $RbGeI_3$, which is lower than those of SnSe (0–10 ps) [59], PbTe (0–10 ps) [60], and GeTe (0.1–9 ps) [61], indicating the lower thermal conductivity in halide perovskites

and corresponding superlattices. Note that $RbGeI_3$ possesses both lower phonon lifetime and phonon group velocities than $CsSnI_3$, resulting in shorter phonon mean free paths (see Fig. S4 in the Supplemental Material [27]). The short phonon mean free paths of $RbGeI_3$ are a reflection of its crystal structures, which contain very distorted GeI_6 octahedra (due to the off-centering Ge atoms), large angle of octahedral tilting, and highly structural inhomogeneity. In the case of $RbGeI_3$, the GeI_6 octahedron contains three very short (2.81, 2.84, and 2.87 Å) and three long (3.08, 3.10, and 3.15 Å) Ge-I bonds, which is observably different from the SnI_6 octahedron (see Fig. S5 in the Supplemental Material [27]). In the Rb-centered polyhedron, the lengths of each Rb-Ge bond and Rb-I bond are different, but in the Cs-centered polyhedron, the same bond length can be found (see Fig. S5 in the Supplemental Material [27]). The highly inhomogeneous bond length map plays a key role in the rattling mechanism, as also proposed by Lee *et al.* [21] for understanding the ultralow thermal conductivity of $CsSnI_3$. Indeed, many studies argued that a similar mechanism is responsible for the low lattice thermal conductivity in clathrates [62] and skutterudites [63,64]. The low phonon lifetime and phonon group velocities are therefore a consequence of the highly inhomogeneous bond length in $RbGeI_3$.

Figures 3(a) and 3(b) present the calculated lattice thermal conductivities (κ_L) of $CsSnI_3$ and $RbGeI_3$ as a function of temperatures. In all cases, the calculated κ_L exhibits distinct anisotropy as a consequence of the crystal symmetry, and $\kappa_{zz} > \kappa_{xx} > \kappa_{yy}$ for all the considered temperatures, where κ_{zz} is the out-of-plane lattice thermal conductivity, and κ_{xx} and κ_{yy} are the in-plane lattice thermal conductivity along the a axis and b axis, respectively. For the $CsSnI_3$ at 300 K, $\kappa_{xx} = 0.388\,\mathrm{W\,m^{-1}\,K^{-1}}$, $\kappa_{yy} = 0.353\,\mathrm{W\,m^{-1}\,K^{-1}}$, $\kappa_{zz} = 0.487\,\mathrm{W\,m^{-1}\,K^{-1}}$, and the average lattice thermal conductivity ($\bar{\kappa}$) is $0.402\,\mathrm{W\,m^{-1}\,K^{-1}}$, which is in good agreement with the experimental values of $0.38 \pm 0.04\,\mathrm{W\,m^{-1}\,K^{-1}}$ [20,21]. For the $RbGeI_3$, $\kappa_{xx} = 0.121\,\mathrm{W\,m^{-1}\,K^{-1}}$, $\kappa_{yy} = 0.107\,\mathrm{W\,m^{-1}\,K^{-1}}$, $\kappa_{zz} = 0.125\,\mathrm{W\,m^{-1}\,K^{-1}}$, and $\bar{\kappa} = 0.117\,\mathrm{W\,m^{-1}\,K^{-1}}$, which are obviously lower than those of $CsSnI_3$. Furthermore, the predicted lattice thermal conductivities of $CsSnI_3$ and $RbGeI_3$ are lower than other thermoelectric materials and traditional oxide perovskites [65,66]. For instance, the lattice thermal conductivities of SnSe [67], Bi_2Te_3 [68], PbTe [4], GeTe [61], $SrZrS_3$ [69], and $PbTiO_3$ [70] are about $0.6\,\mathrm{W\,m^{-1}\,K^{-1}}$, $0.7\,\mathrm{W\,m^{-1}\,K^{-1}}$, $2.2\,\mathrm{W\,m^{-1}\,K^{-1}}$, $2.7\,\mathrm{W\,m^{-1}\,K^{-1}}$, $1.26\,\mathrm{W\,m^{-1}\,K^{-1}}$, and $5\,\mathrm{W\,m^{-1}\,K^{-1}}$, respectively. The ultralow κ_L is the consequence of the ultralow phonon group velocities of low-mid-frequency high-density phonon modes and ultrashort phonon lifetime of all phonon modes (Fig. 2).

The $RbGeI_3/CsSnI_3$ superlattices adopt a lower symmetry (Pc) than the parent structure $RbGeI_3$ ($Pna2_1$) and $CsSnI_3$ ($Pnma$). Thus, the superlattices would exhibit more complex phonon dispersion and phonon-phonon coupling than those in the parent structure [14,21] and possess low lattice thermal conductivity. Because the in-plane transport properties of $RbGeI_3/CsSnI_3$ superlattices with different superlattice periods are the focus of our investigation, we calculate the in-plane lattice thermal conductivity of each
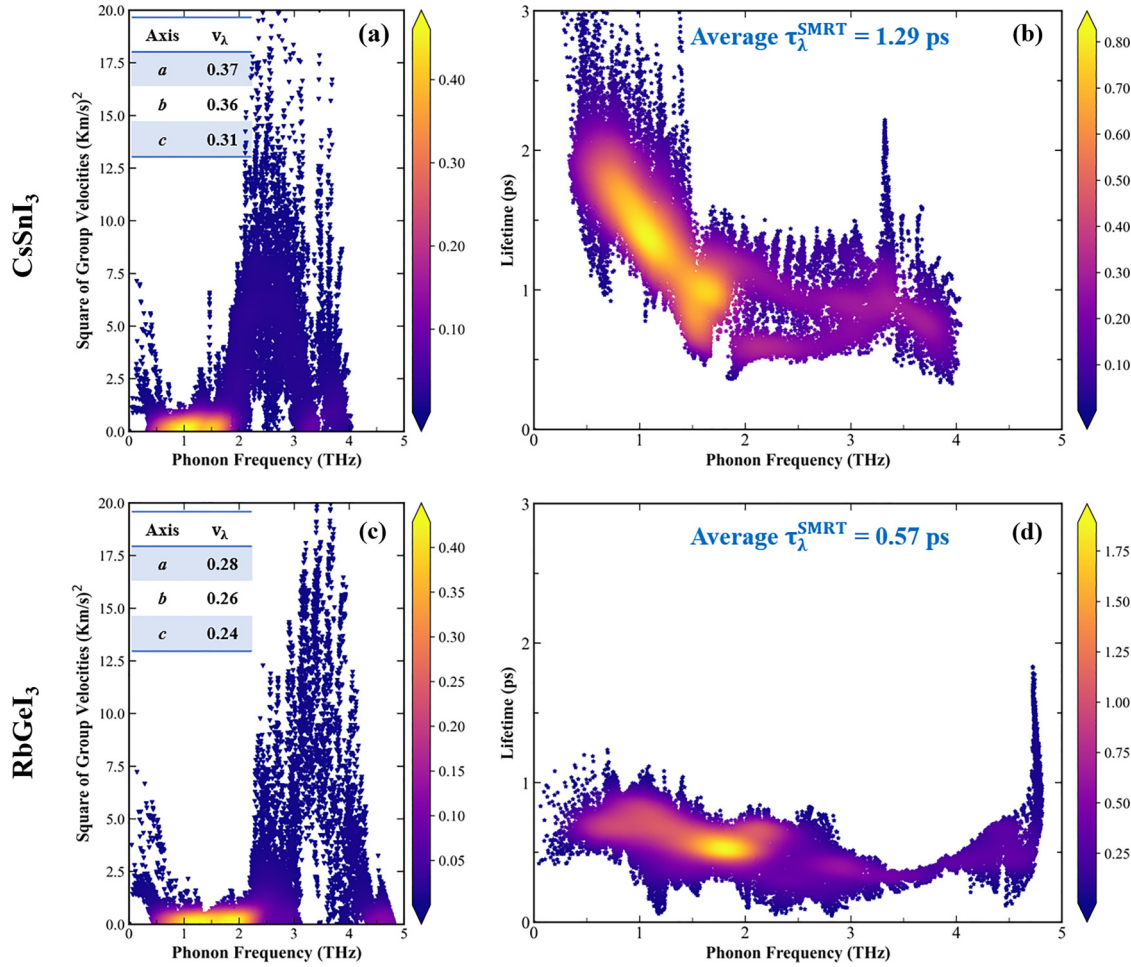
FIG. 2. Phonon transport properties. (a),(c) The square of phonon group velocities, and (b),(d) phonon lifetime at 300 K for $CsSnI_3$ (top panels) and $RbGeI_3$ (bottom panels). The symbols in the figures symbolize the phonon modes. The colored background represents the density of the phonon modes and the brighter color means a higher density. The insets in panels (a) and (c) are the average phonon group velocities along the a, b, and c axes, respectively. The insets in panels (b) and (d) are the average phonon lifetime.

$(RbGeI_3)_m/(CsSnI_3)_n$ ($m + n = 6$) superlattice, as shown in Fig 3(c). We find that the in-plane lattice thermal conductivity decreases with decreasing thickness of $CsSnI_3$ layers in the $RbGeI_3/CsSnI_3$ superlattices (from 1/5 SL to 5/1 SL). For the $(RbGeI_3)_1/(CsSnI_3)_5$ superlattice, the in-plane lattice thermal conductivity is 0.181 W m^{-1} K^{-1} at 300 K. For

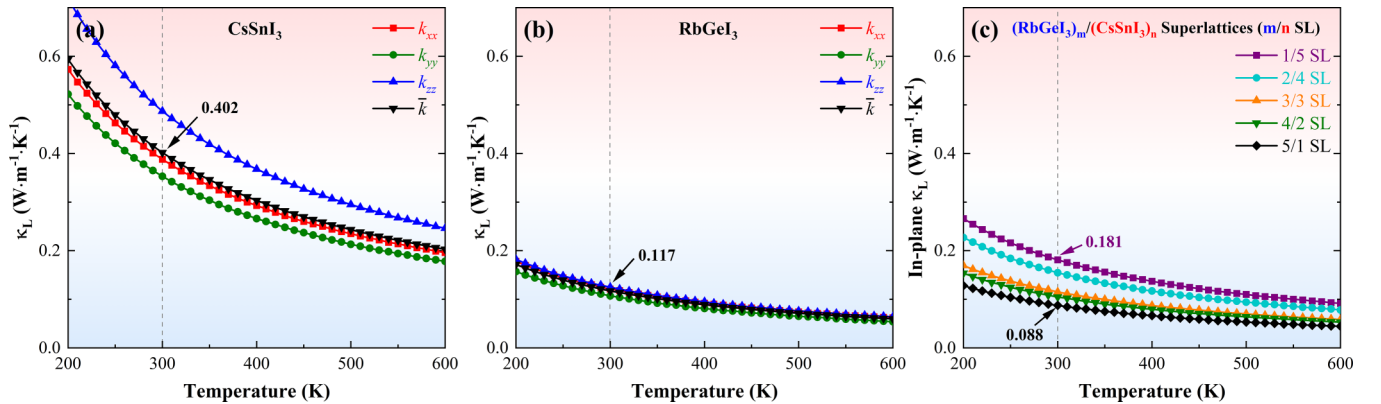
FIG. 3. Lattice thermal conductivity. The calculated temperature-dependent lattice thermal conductivity (κ_L) of (a) $CsSnI_3$, (b) $RbGeI_3$, and (c) $(RbGeI_3)_m/(CsSnI_3)_n$ superlattices ($m = 1 \ldots 5$; $n = 5 \ldots 1$; $m + n = 6$). The κ_{xx}, κ_{yy}, and κ_{zz} represent the κ_L along the a, b, and c directions, respectively. The $\bar{\kappa}$ is the average lattice thermal conductivity. The in-plane κ_L is the average lattice thermal conductivity of κ_{xx} and κ_{yy}. The vertical line indicates the κ_L at 300 K. The red and blue backgrounds indicate high thermal conductivity and low thermal conductivity, respectively.
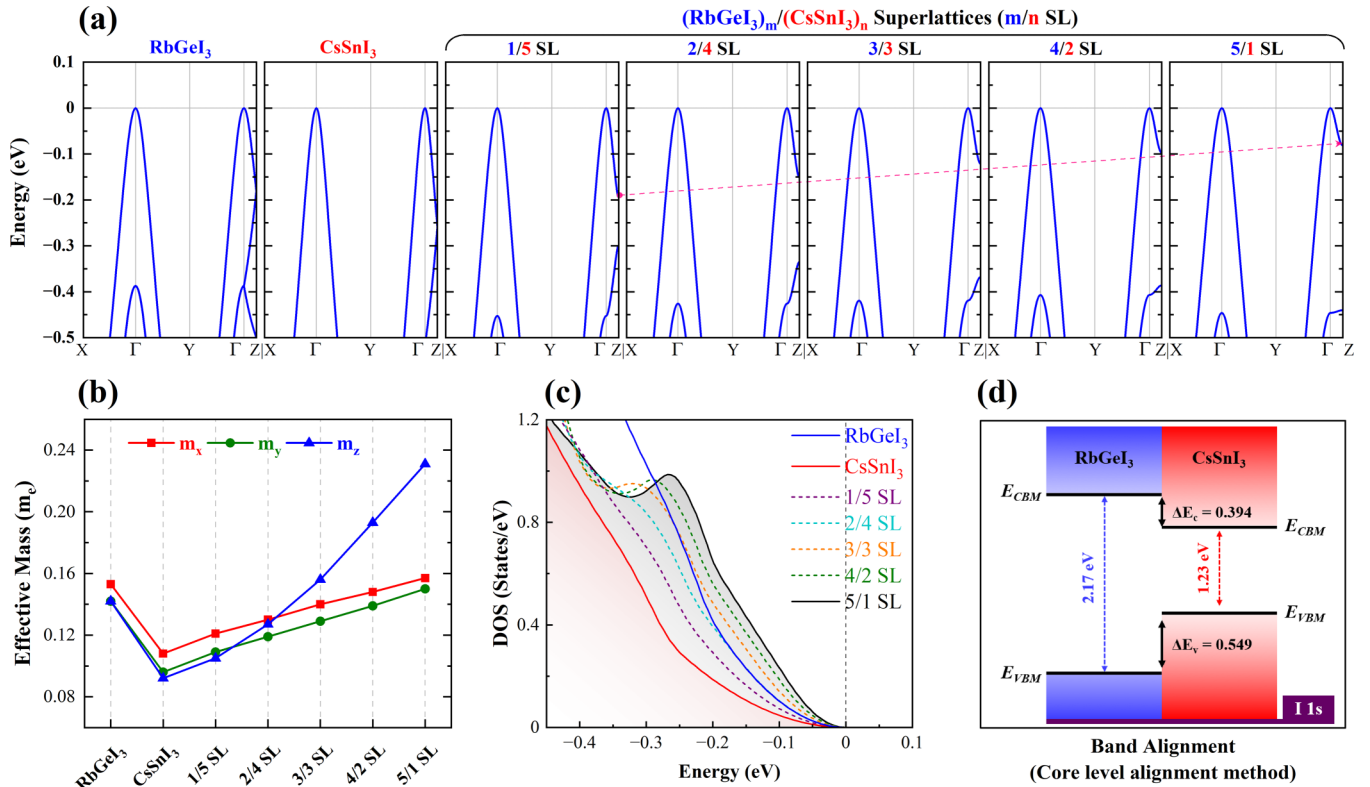
FIG. 4. Electronic structure. (a) Calculated valence band structures, (b) effective mass, and (c) density of states for $RbGeI_3$, $CsSnI_3$, and $(RbGeI_3)_m/(CsSnI_3)_n$ superlattices ($m = 1\ldots5$; $n = 5\ldots1$; $m + n = 6$). (d) Sketch of the alignment of the valence band maximum (VBM) and conduction band maximum (CBM) energies of $RbGeI_3$ and $CsSnI_3$. Note that the energies in panel (d) are calculated by HSE06. In panels (a) and (c), the valence band maximum is set to 0. The effective masses m_x, m_y, and m_z were estimated from quadratic fits of the bands along the directions Γ to X, Γ to Y, and Γ to Z, respectively.

the $(RbGeI_3)_5/(CsSnI_3)_1$ superlattice, it is $0.088\,\mathrm{W\,m^{-1}\,K^{-1}}$. These results of low thermal conductivity in superlattices and interfaces were observed in both experimental [71–73] and theoretical studies [74,75].

C. Electronic structure and quantum-confinement effect

Figure 4(a) shows the electronic structures of $RbGeI_3$, $CsSnI_3$, and $RbGeI_3/CsSnI_3$ superlattices. Only the valence bands near the Fermi level are shown. One can see that the in-plane bands along Γ-X and Γ-Y are very similar, while the maximum valence state and the second valence state at the Z point shifts to higher and lower energy, respectively, with decreasing the $CsSnI_3$ layers in $RbGeI_3/CsSnI_3$ superlattices. Note that the band energy shifting upwards/downwards at the Z point is induced by the reduced thickness of $CsSnI_3$ layers (even reduced to a two-dimensional structure) which flattens the band mainly coming from $CsSnI_3$ along Γ-Z. In other words, the energy at the Z point of the band coming from $CsSnI_3$ would shift to the energy of the Γ point of this band, and the bands along Γ-Z become flat. This energy shift of state at the Z point leads to the corresponding reduction of band curvature along Γ-Z, and thus the effective mass along Γ-Z becomes large with the decreased $CsSnI_3$ layers in the superlattice, as shown in Fig. 4(b) and Supplemental Material Table S2 [27]. As illustrated in Fig. 4(c), the DOS near the

Fermi level increases with decreasing amount of $CsSnI_3$ in the superlattices (from 1/5 SL to 5/1 SL).

In a quantum-well heterojunction, the band alignment of the interface can be determined by the core-level alignment scheme [76,77]. We thus use the average energies of $1s$ orbitals of all I atoms as the core level and the reference energy. Comparing the band structure of $RbGeI_3$ and $CsSnI_3$, the valence band offset (ΔE) between $RbGeI_3$ and $CsSnI_3$ is 0.549 eV with the valence band maximum of $CsSnI_3$ lying higher than that of $RbGeI_3$ [see Fig. 4(d)], which is calculated by HSE06 [78]. A similar valence band offset is also found in PBEsol calculations (see Fig. S6 in the Supplemental Material [27]) but is different in specific values. Our calculated band offset of $RbGeI_3/CsSnI_3$ (0.549 eV) is far larger than that of Bi_2Te_3/Sb_2Te_3 (0.035 eV) [79], $SrTe/PbTe$ (0.06 eV) [80], PbS/CdS (0.13 eV) [81], and $PbTe/Pb_{0.927}Eu_{0.073}Te$ superlattice (0.2 eV) [36]. The large band offset in the valence band edges is high enough to set up large potential barriers in the superlattices, which can lead to strong confinement of the hole transport in the $CsSnI_3$ well region that benefits the thermoelectric performance [82].

Low-dimensional hole transport requires the low-dimensional electronic structure and valence band maximum (VBM); we therefore examined the layer-resolved densities of state (LDOS) of superlattices, as shown in Fig. 5, together with the LDOS of bulk $RbGeI_3$ and $CsSnI_3$ for comparison. In bulk $RbGeI_3$ and $CsSnI_3$, the valence states near the Fermi
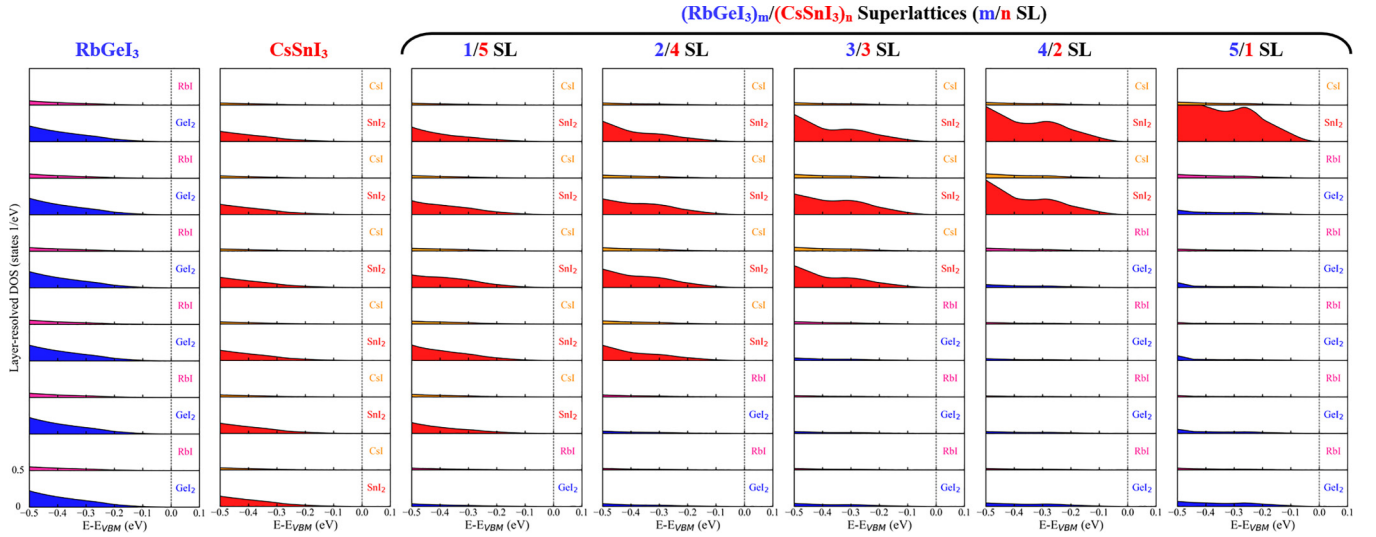
FIG. 5. Layer-resolved electronic structure. Layer-resolved electronic density of states (LDOS) for $RbGeI_3$, $CsSnI_3$, and $(RbGeI_3)_m/(CsSnI_3)_n$ superlattices ($m = 1 \ldots 5$; $n = 5 \ldots 1$; $m + n = 6$).

level are mainly from Ge, Sn, and I atoms, and the *A*-site atoms (Rb and Cs) do not contribute to the valence states. Interestingly, in the cases of $RbGeI_3/CsSnI_3$ superlattices, the valence states near the Fermi level are only from SnI_2 atomic layers, and $RbGeI_3$ does not contribute to the states near the Fermi level (band and DOS in a broad energy range; see Fig. S7 in the Supplemental Material [27]), implying that the hole carriers are confined in $Sn-I_2$ atomic layers. This is similar to the charge transport behavior exhibited in the engineering of band alignment at perovskite solar cells that have been extensively reported [13,83,84]. Additionally, as the $CsSnI_3$ layer thickness decreases in the $RbGeI_3/CsSnI_3$ superlattices, the densities of state near the VBM of each $Sn-I_2$ atomic layer increase. The electronic structures clearly show that $RbGeI_3/CsSnI_3$ superlattices exhibit a multiple quantum well composed of $(RbGeI_3)_m$ (barrier)/$(CsSnI_3)_n$ (well) having a strong hole carrier quantum-confinement effect.

D. Thermoelectric properties

To evaluate the thermoelectric performance ($ZT = S^2\sigma T/(\kappa_{ele} + \kappa_L)$), we then consider the electronic transport properties of the Seebeck coefficient (S), electrical conductivity (σ), power factor (PF; $S^2\sigma$), and electronic thermal conductivity (κ_{ele}). These electronic transport properties can be calculated by solving the electronic Boltzmann transport equation within the relaxation-time approximation (see Note 1 in the Supplemental Material [27]). In solving the electronic Boltzmann transport equation, choosing a reasonable relaxation time for carriers is crucial to compute the electrical conductivity, power factor, electronic thermal conductivity, and figure of merit ZT. Here, the relaxation time was chosen to be 20 fs (at 300 K), which was determined by fitting the calculated electrical conductivity in the experiments of $CsSnI_3$ system [21]. To validate the relaxation time (20 fs) and our computation methodology, we evaluated the thermoelectric properties of bulk $CsSnI_3$ (see Fig. S8 in the Supplemental Material [27]) and the calculated results are in good agreement

with experimental values [21]. The required parameters to obtain the thermoelectric properties are given in Supplemental Material Table S3 [27].

We calculated the Seebeck coefficient, electrical conductivity, power factor, and ZT in the [100] and [010] (in-plane) directions, as well as in the [001] (out-of-plane) direction for all $RbGeI_3/CsSnI_3$ superlattices. The average in-plane thermoelectric properties of the $RbGeI_3/CsSnI_3$ superlattices are displayed in Fig. 6. As shown in Fig. 6(a), we find that the in-plane Seebeck coefficient (S_{ab}) of all $RbGeI_3/CsSnI_3$ superlattices is larger than that of $CsSnI_3$. Furthermore, the S_{ab} increases with decreasing thickness of $CsSnI_3$ layers in the $RbGeI_3/CsSnI_3$ superlattices (from 1/5 SL to 5/1 SL), which is mainly induced by the increase of the density of state near the Fermi level [8,85,86] [see Fig. 4(c)]. Unlike the S_{ab}, the calculated in-plane electrical conductivity (σ_{ab}) of superlattices is lower than that of $CsSnI_3$. Therefore, the σ_{ab} of the superlattices has a negative contribution to the ZT, compared to the parent materials.

The improved S_{ab} in superlattices results in the enhancement of the in-plane power factor (PF$_{ab}$, $S^2\sigma$) at the carrier concentrations of 10^{17}–3×10^{19} cm^{-3}, though σ_{ab} tends to reduce PF$_{ab}$. In these carrier concentrations, the maximum PF$_{ab}$ of $CsSnI_3$ at 300 K is 184 µW m^{-1} K^{-2} [Fig. 6(c)]. For the $(RbGeI_3)_m/(CsSnI_3)_n$ superlattices, the maximum PF$_{ab}$ is 203 µW m^{-1} K^{-2} for 1/5 SL and it increases with the decrease of thickness of the $CsSnI_3$ layer in the superlattice, and it is 360 µW m^{-1} K^{-2} for the 5/1 superlattice [Fig. 6(c)]. Figure 6(d) shows the in-plane figure of merit (ZT_{ab}). Because of the lower lattice thermal conductivity, the ZT_{ab} for superlattices is obviously improved. The maximum ZT_{ab} of $CsSnI_3$ is only 0.15. The maximum ZT_{ab} for superlattices increases with the decrease of $CsSnI_3$ layers in superlattices. It is 1.34 of 5/1 SL at a hole doping concentration of 5.0×10^{18} cm^{-3}, which is the highest for any $CsSnI_3$-based compounds. We numerically find that the maximum PF$_{ab}$ and ZT_{ab} of 5/1 SL are about two times and nine times those of $CsSnI_3$, respectively. A similar enhanced phenomenon was observed in the Bi_2Te_3
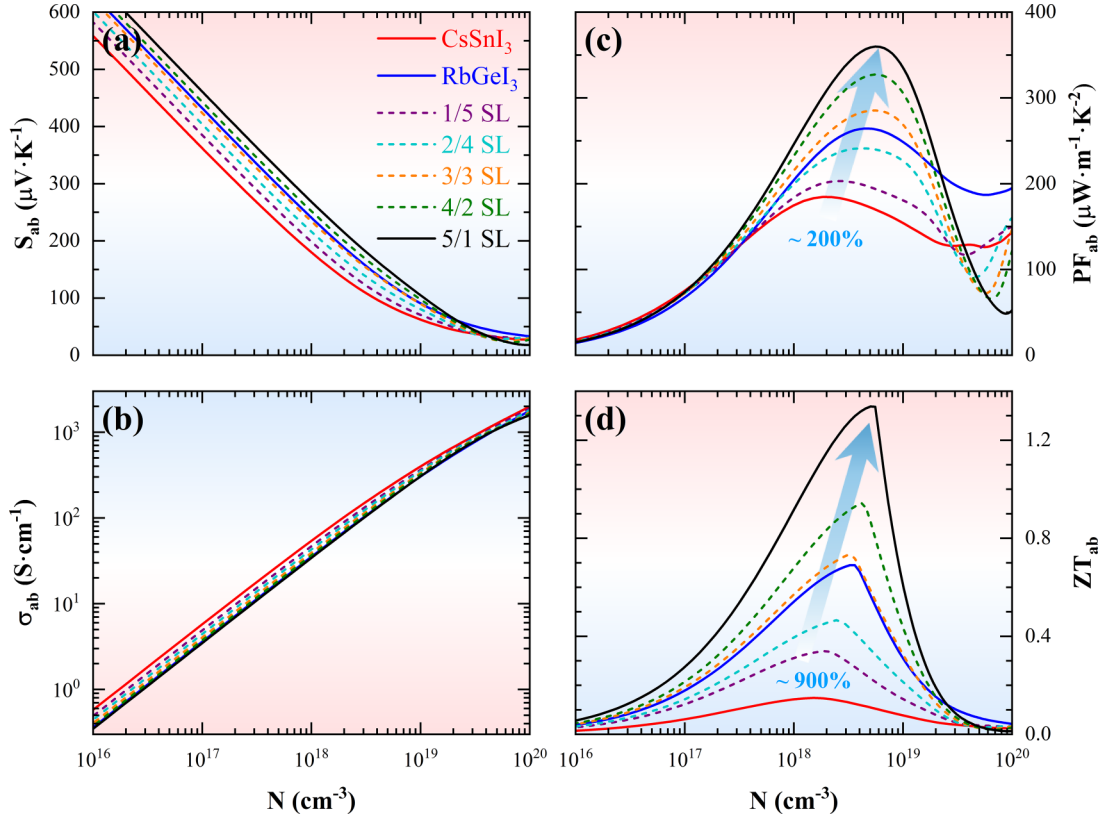
FIG. 6. In-plane thermoelectric properties. The thermoelectric properties of $RbGeI_3$, $CsSnI_3$, and $(RbGeI_3)_m/(CsSnI_3)_n$ superlattices ($m = 1 \ldots 5$; $n = 5 \ldots 1$; $m + n = 6$) along the in-plane direction under hole doping at 300 K. (a) The Seebeck coefficient S_{ab}. (b) The electrical conductivity σ_{ab}. (c) The power factor PF_{ab}. (d) The figure of merit ZT_{ab}. The blue fading into red indicates the changed thermoelectric properties with decreasing thickness of $CsSnI_3$ layers in the $RbGeI_3/CsSnI_3$ superlattices (from 1/5 SL to 5/1 SL).

quantum wells [30,87]. The increase in *ZT* with decreasing the quantum-well thickness is caused by the bound motion in two dimensions, which can be explained by the single parabolic band model (see Note 2 in the Supplemental Material [27]).

As a supplemental confirmation, we also consider the case of different total layers ($m + n$) of $(RbGeI_3)_m/(CsSnI_3)_n$ superlattices, and similar results of thermoelectric properties are still observed (see Supplemental Material Fig. S9 [27]). By comparing the cases of $(RbGeI_3)_m/(CsSnI_3)_1$ superlattices ($m = 1, 3, 5, 7, 9$), we find that the maximum PF_{ab} increases first and then decreases. The 5/1 SL possesses the best thermoelectric performance owing to the highest valence states near the Fermi level (Supplemental Material Fig. S10 [27]). This indicates that the gain of thermoelectric performance in the confined region can be partly counterbalanced by the contribution from the $RbGeI_3$ barrier material which produces the confinement, similar to what was proposed by Bilc *et al.* [88]. Therefore, the key to obtaining the optimal *ZT* is to prepare the appropriate quantum-well superlattice.

Figure 7(a) shows the predicated ZT_{ab} of 5/1 SL as a function carrier concentration at temperatures of 300, 400, 500, and 550 K. *ZT* increases with the increase of temperature. The carrier concentration at which *ZT* is the maximum remains at about 9.0×10^{18} cm^{-3} for any considered temperature, enabling a self-optimized ZT_{ab} at different temperatures in a single material without changing the actual doping levels

[89,90]. The maximum ZT_{ab} is 3.78 at 550 K, much larger than that (0.15) of *p*-type doping of $CsSnI_3$ [19]. Fig. 7(b) shows the ZT of 5/1 SL at different temperatures compared to that of other thermoelectric materials [3,91–105]. 5/1 SL exhibits the largest *ZT* at a temperature larger than 300 K. These high *ZT*s combined with the stabilized optimal carrier concentration, make the 5/1 SL a promising material for room-temperature thermoelectric applications.

IV. SUMMARY

In summary, we investigated the thermoelectric properties of $RbGeI_3/CsSnI_3$ superlattices by utilizing the first-principles method combined with the Boltzmann transport theory. The $CsSnI_3$ and $RbGeI_3$ possess ultralow lattice thermal conductivities of 0.402 and 0.117 W m^{-1} K^{-1} at 300 K, respectively. The latter is lower because it holds a significantly reduced phonon lifetime, resulting from ferroelectric instability. Exploiting the quantum-confinement effects, we selected the $RbGeI_3$ as the barrier material for the $CsSnI_3$ quantum well in preparing $RbGeI_3/CsSnI_3$ superlattices. As a consequence, we achieved low-dimensional hole transport, thereby resulting in an increase in the in-plane power factor and *ZT*. In the $RbGeI_3/CsSnI_3$ superlattices, the in-plane power factor and *ZT* increase with decreasing the $CsSnI_3$ well thickness. The in-plane power factor and *ZT* of the $(RbGeI_3)_5/(CsSnI_3)_1$ superlattice are about two times and nine times those of $CsSnI_3$,
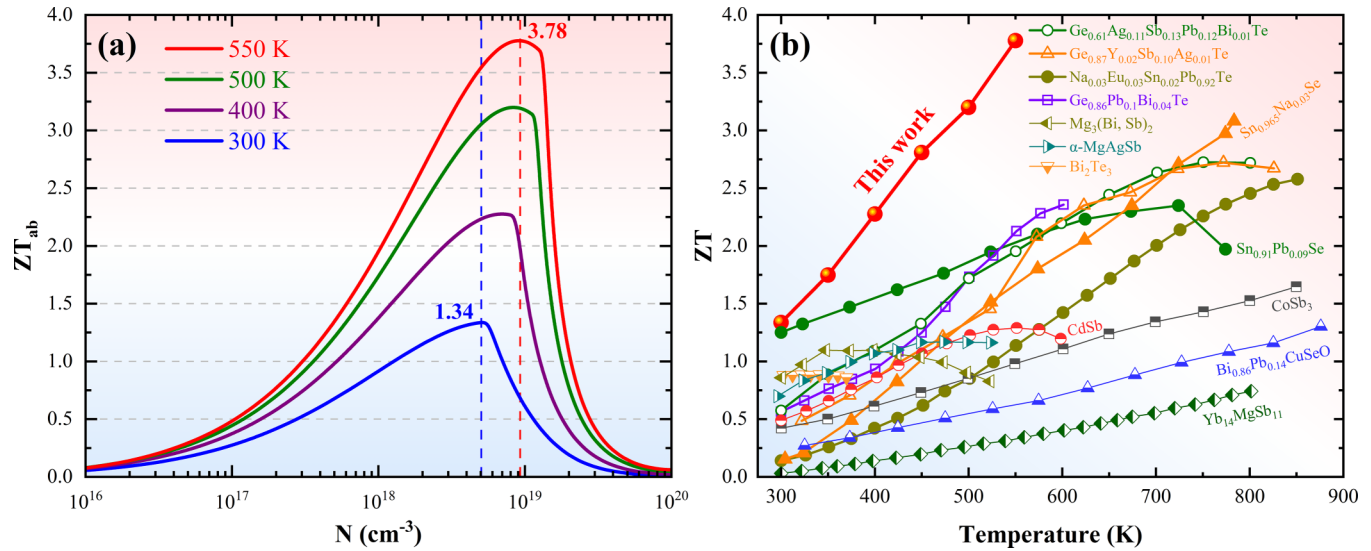
FIG. 7. The dimensionless figure of merit ZT of 5/1 SL. (a) The predicated in-plane ZT_{ab} values of $(RbGeI_3)_5/(CsSnI_3)_1$ superlattice as a function of carrier concentration at temperatures of 300, 400, 500, and 550 K. The blue and red vertical lines represent the optimal carrier concentration N^* (where the ZT peaks) at 300 and 550 K, respectively. (b) Temperature dependence of ZT for various thermoelectric materials. The red balls represent the results of 5/1 superlattice. The ZT information of other materials comes from Refs. [3,91–105]. The red and blue backgrounds indicate high ZT and low ZT, respectively.

respectively. We unveiled that the $(RbGeI_3)_5/(CsSnI_3)_1$ superlattices possess the high ZT (1.34 at 300 K and 3.78 at 550 K), which is promising for room-temperature thermoelectric applications. In a word, our current findings unveiled the critical role of the quantum-confinement effects in enhancing thermoelectric properties, which will provide useful information for further experimental and theoretical studies on $CsSnI_3$ and other related halide perovskite superlattice materials.

[1] Q. Yang, S. Yang, P. Qiu, L. Peng, T.-R. Wei, Z. Zhang, X. Shi, and L. Chen, Flexible thermoelectrics based on ductile semiconductors, Science **377**, 854 (2022).

[2] X. Shi and L. Chen, Thermoelectric materials step up, Nat. Mater. **15**, 691 (2016).

[3] B. Qin, D. Wang, X. Liu, Y. Qin, J.-F. Dong, J. Luo, J.-W. Li, W. Liu, G. Tan, X. Tang, J.-F. Li, J. He, and L.-D. Zhao, Power generation and thermoelectric cooling enabled by momentum and energy multiband alignments, Science **373**, 556 (2021).

[4] Y. Pei, X. Shi, A. LaLonde, H. Wang, L. Chen, and G. J. Snyder, Convergence of electronic bands for high performance bulk thermoelectrics, Nature (London) **473**, 66 (2011).

[5] X. Zhang and Y. Pei, Manipulation of charge transport in thermoelectrics, npj Quantum Mater. **2**, 68 (2017).

[6] Y. Tang, Z. M. Gibbs, L. A. Agapito, G. Li, H.-S. Kim, M. B. Nardelli, S. Curtarolo, and G. J. Snyder, Convergence of multi-valley bands as the electronic origin of high thermoelectric performance in $CoSb_3$ skutterudites, Nat. Mater. **14**, 1223 (2015).

[7] Z. Chen, X. Zhang, and Y. Pei, Manipulation of phonon transport in thermoelectrics, Adv. Mater. **30**, 1705617 (2018).

[8] Y. Xiao and L. D. Zhao, Charge and phonon transport in PbTe-based thermoelectric materials, npj Quantum Mater. **3**, 55 (2018).

[9] H. Zhou, Q. Chen, G. Li, S. Luo, T.-B. Song, H.-S. Duan, Z. Hong, J. You, Y. Liu, and Y. Yang, Interface engineering of highly efficient perovskite solar cells, Science **345**, 542 (2014).

[10] A. Pisoni, J. Jacimovic, O. S. Barisic, M. Spina, R. Gaal, L. Forro, and E. Horvath, Ultra-low thermal conductivity in organic-inorganic hybrid perovskite $CH_3NH_3PbI_3$, J. Phys. Chem. Lett. **5**, 2488 (2014).

[11] Q. Dong, Y. Fang, Y. Shao, P. Mulligan, J. Qiu, L. Cao, and J. Huang, Electron-hole diffusion lengths >175 9.83 μm in solution-grown $CH_3NH_3PbI_3$ single crystals, Science **347**, 967 (2015).

[12] F. Hao, C. C. Stoumpos, C. Duyen Hanh, R. P. H. Chang, and M. G. Kanatzidis, Lead-free solid-state organic-inorganic halide perovskite solar cells, Nat. Photon. **8**, 489 (2014).

[13] J. Deng, S. Yuan, H. Xiong, Z. Ma, W. Wu, M. Wang, Z. Lou, J. Fan, and W. Li, Br-I ordered $CsPbBr_2I$ perovskite single crystal toward extremely high mobility, Chem **9**, 1929 (2023).

[14] Y. He and G. Galli, Perovskites for solar thermoelectric applications: A first principle study of $CH_3NH_3AI_3$ (A = Pb and Sn), Chem. Mater. **26**, 5394 (2014).

[15] X. Mettan, R. Pisoni, P. Matus, A. Pisoni, J. Jaamovic, B. Nafradi, M. Spina, D. Pavuna, L. Forro, and E. Horvath, Tuning of the thermoelectric figure of merit of $CH_3NH_3MI_3$ (M = Pb, Sn) photovoltaic perovskites, J. Phys. Chem. C **119**, 11506 (2015).

[16] L. Yan, M. Wang, C. Zhai, L. Zhao, and S. Lin, Symmetry breaking induced anisotropic carrier transport and remarkable thermoelectric performance in mixed halide perovskites $CsPb(I_{1-x}Br_x)_3$, ACS Appl. Mater. Interfaces **12**, 40453 (2020).

[17] U. G. Jong, C. J. Yu, Y. H. Kye, S. N. Hong, and H. G. Kim, Manifestation of the thermoelectric properties in Ge-based halide perovskites, Phys. Rev. Mater. **4**, 075403 (2020).

[18] U.-G. Jong, Y.-S. Kim, C.-H. Ri, Y.-H. Kye, and C.-J. Yu, High thermoelectric performance in the cubic inorganic cesium iodide perovskites $CsBI_3$ (B = Pb, Sn, and Ge) from first-principles, J. Phys. Chem. C **125**, 6013 (2021).

[19] H. Xie, S. Hao, J. Bao, T. J. Slade, G. J. Snyder, C. Wolverton, and M. G. Kanatzidis, All-inorganic halide perovskites as potential thermoelectric materials: Dynamic cation off-centering induces ultralow thermal conductivity, J. Am. Chem. Soc. **142**, 9553 (2020).

[20] T. Liu, X. Zhao, J. Li, Z. Liu, F. Liscio, S. Milita, B. C. Schroeder, and O. Fenwick, Enhanced control of self-doping in halide perovskites for improved thermoelectric performance, Nat. Commun. **10**, 5750 (2019).

[21] W. Lee, H. Li, A. B. Wong, D. Zhang, M. Lai, Y. Yu, Q. Kong, E. Lin, J. J. Urban, J. C. Grossman, and P. Yang, Ultralow thermal conductivity in all-inorganic halide perovskites, Proc. Natl. Acad. Sci. USA **114**, 8693 (2017).

[22] I. Chung, J.-H. Song, J. Im, J. Androulakis, C. D. Malliakas, H. Li, A. J. Freeman, J. T. Kenney, and M. G. Kanatzidis, $CsSnI_3$: Semiconductor or metal? High electrical conductivity and strong near-infrared photoluminescence from a single material. high hole mobility and phase-transitions, J. Am. Chem. Soc. **134**, 8579 (2012).

[23] T. Wang, X. Xu, W. Li, Y. Li, Q. Liu, C. Li, C. Shan, G. Li, T. Shi, and A. K. K. Kyaw, Simultaneous enhancement of thermoelectric power factor and phase stability of tin-based perovskites by organic cation doping, ACS Appl. Energy Mater. **5**, 11191 (2022).

[24] F. Qian, M. Hu, J. Gong, C. Ge, Y. Zhou, J. Guo, M. Chen, Z. Ge, N. P. Padture, Y. Zhou, and J. Feng, Enhanced thermoelectric performance in lead-free inorganic $CsSn_{1-x}Ge_xI_3$ perovskite semiconductors, J. Phys. Chem. C **124**, 11749 (2020).

[25] S. Hu, Z. Ren, A. B. Djurisc, and A. L. Rogach, Metal halide perovskites as emerging thermoelectric materials, ACS Energy Lett. **6**, 3882 (2021).

[26] S. Yu, F. Qian, M. Hu, Z. Ge, J. Feng, and X. Chong, Enhanced thermoelectric performance in inorganic $CsSnI_3$ perovskite by doping with PbI_2, Mater. Lett. **308**, 131127 (2022).

[27] See Supplemental Material at http://link.aps.org/supplemental/10.1103/PhysRevB.109.085305 for details about the results as well as additional information.

[28] G. K. H. Madsen, J. Carrete, and M. J. Verstraete, BoltzTraP2, A program for interpolating band structures and calculating semi-classical transport coefficients, Comput. Phys. Commun. **231**, 140 (2018).

[29] A. M. Ganose, J. Park, A. Faghaninia, R. Woods-Robinson, K. A. Persson, and A. Jain, Efficient calculation of carrier scattering rates from first principles, Nat. Commun. **12**, 2222 (2021).

[30] L. D. Hicks and M. S. Dresselhaus, Effect of quantum-well structures on the thermoelectric figure of merit, Phys. Rev. B **47**, 12727 (1993).

[31] M. S. Dresselhaus, G. Chen, M. Y. Tang, R. Yang, H. Lee, D. Wang, Z. Ren, J.-P. Fleurial, and P. Gogna, New directions for low-dimensional thermoelectric materials, Adv. Mater. **19**, 1043 (2007).

[32] A. K. Baranwal, S. Saini, Z. Wang, D. Hirotani, T. Yabuki, S. Iikubo, K. Miyazaki, and S. Hayase, Interface engineering using Y_2O_3 scaffold to enhance the thermoelectric performance of $CsSnI_3$ thin film, Org. Electron. **76**, 105488 (2020).

[33] W. Tang, T. Liu, and O. Fenwick, High thermoelectric performance based on $CsSnI_3$ thin films with improved stability, J. Mater. Chem. A **10**, 7020 (2022).

[34] A. K. Baranwal, S. Saini, Y. Sanehira, G. Kapil, M. A. Kamarudin, C. Ding, S. R. Sahamir, T. Yabuki, S. Iikubo, Q. Shen, K. Miyazaki, and S. Hayase, Unveiling the role of the metal oxide/Sn perovskite interface leading to low efficiency of Sn-perovskite solar cells but providing high thermoelectric properties, ACS Appl. Energy Mater. **5**, 9750 (2022).

[35] L. D. Hicks, T. C. Harman, X. Sun, and M. S. Dresselhaus, Experimental study of the effect of quantum-well structures on the thermoelectric figure of merit, Phys. Rev. B **53**, 010493(R) (1996).

[36] T. C. Harman, D. L. Spears, and M. J. Manfra, High thermoelectric figures of merit in PbTe quantum wells, J. Electron. Mater. **25**, 1121 (1996).

[37] H. Ohta, S. Kim, Y. Mune, T. Mizoguchi, K. Nomura, S. Ohta, T. Nomura, Y. Nakanishi, Y. Ikuhara, M. Hirano, H. Hosono, and K. Koumoto, Giant thermoelectric Seebeck coefficient of two-dimensional electron gas in $SrTiO_3$, Nat. Mater. **6**, 129 (2007).

[38] W. S. Choi, H. Ohta, S. J. Moon, Y. S. Lee, and T. W. Noh, Dimensional crossover of polaron dynamics in $Nb:SrTiO_3/SrTiO_3$ superlattices: Possible mechanism of thermopower enhancement, Phys. Rev. B **82**, 024301 (2010).

[39] B. Geisler and R. Pentcheva, Inducing n- and p-type thermoelectricity in oxide superlattices by strain tuning of orbital-selective transport resonances, Phys. Rev. Appl. **11**, 044047 (2019).

[40] B. Geisler and R. Pentcheva, Confinement- and strain-induced enhancement of thermoelectric properties in $LaNiO_3/LaAlO_3$ (001) superlattices, Phys. Rev. Mater. **2**, 055403 (2018).

[41] B. Geisler, A. Blanca-Romero, and R. Pentcheva, Design of n- and p-type oxide thermoelectrics in $LaNiO_3/SrTiO_3$(001) superlattices exploiting interface polarity, Phys. Rev. B **95**, 125301 (2017).

[42] P. Garcia-Fernandez, M. Verissimo-Alves, D. I. Bilc, P. Ghosez, and J. Junquera, First-principles modeling of the thermoelectric properties of $SrTiO_3/SrRuO_3$ superlattices, Phys. Rev. B **86**, 085305 (2012).

[43] I. Pallecchi, F. Telesio, D. Li, A. Fete, S. Gariglio, J.-M. Triscone, A. Filippetti, P. Delugas, V. Fiorentini, and D.

Marre, Giant oscillating thermopower at oxide interfaces, Nat. Commun. **6**, 6678 (2015).

[44] P. Delugas, A. Filippetti, M. J. Verstraete, I. Pallecchi, D. Marre, and V. Fiorentini, Doping-induced dimensional crossover and thermopower burst in Nb-doped $SrTiO_3$ superlattices, Phys. Rev. B **88**, 045310 (2013).

[45] M. Verma, B. Geisler, and R. Pentcheva, Effect of confinement and octahedral rotations on the electronic, magnetic, and thermoelectric properties of correlated $SrXO_3/SrTiO_3$ (001) superlattices ($X = $ V, Cr, or Mn), Phys. Rev. B **100**, 165126 (2019).

[46] M. Verma and R. Pentcheva, Metal-insulator transition and robust thermoelectricity via strain-tuned interplay between structural and electronic properties in $(SrVO_3)_1/(SrTiO_3)_1$ (001) superlattices, Phys. Rev. Res. **4**, 033013 (2022).

[47] Y. Luo, H. Tian, X. Li, L. Chen, Y. Yang, and D. Wu, Diversity of structural phases in $AGeX_3$ halides, Phys. Rev. B **106**, 024112 (2022).

[48] G. Kresse and J. Furthmüller, Efficient iterative schemes for *ab initio* total-energy calculations using a plane-wave basis set, Phys. Rev. B **54**, 11169 (1996).

[49] G. Kresse and J. Furthmuller, Efficiency of ab-initio total energy calculations for metals and semiconductors using a plane-wave basis set, Comput. Mater. Sci. **6**, 15 (1996).

[50] J. P. Perdew, A. Ruzsinszky, G. I. Csonka, O. A. Vydrov, G. E. Scuseria, L. A. Constantin, X. Zhou, and K. Burke, Restoring the density-gradient expansion for exchange in solids and surfaces, Phys. Rev. Lett. **100**, 136406 (2008).

[51] K. F. Garrity, First-principles search for *n*-type oxide, nitride, and sulfide thermoelectrics, Phys. Rev. B **94**, 045122 (2016).

[52] A. Togo and I. Tanaka, First principles phonon calculations in materials science, Scr. Mater. **108**, 1 (2015).

[53] A. Togo, L. Chaput, and I. Tanaka, Distributions of phonon lifetimes in Brillouin zones, Phys. Rev. B **91**, 094306 (2015).

[54] C. Wang, Y. B. Chen, S.-H. Yao, and J. Zhou, Low lattice thermal conductivity and high thermoelectric figure of merit in Na_2MgSn, Phys. Rev. B **99**, 024310 (2019).

[55] E. Osei-Agyemang, C. E. Adu, and G. Balasubramanian, Ultralow lattice thermal conductivity of chalcogenide perovskite $CaZrSe_3$ contributes to high thermoelectric figure of merit, npj Comput. Mater. **5**, 116 (2019).

[56] R. M. Pick, M. H. Cohen, and R. M. Martin, Microscopic theory of force constants in the adiabatic approximation, Phys. Rev. B **1**, 910 (1970).

[57] A. M. Glazer, The classification of tilted octahedra in perovskites, Acta Crystallogr., Sect. B: Struct. Sci., Cryst. Eng. Mater. **28**, 3384 (1972).

[58] L. Chen, C. S. Xu, H. Tian, H. J. Xiang, J. Iniguez, Y. R. Yang, and L. Bellaiche, Electric-field control of magnetization, Jahn-Teller distortion, and orbital ordering in ferroelectric ferromagnets, Phys. Rev. Lett. **122**, 247701 (2019).

[59] R. Guo, X. Wang, Y. Kuang, and B. Huang, First-principles study of anisotropic thermoelectric transport properties of IV-VI semiconductor compounds SnSe and SnS, Phys. Rev. B **92**, 115202 (2015).

[60] Z. Tian, J. Garg, K. Esfarjani, T. Shiga, J. Shiomi, and G. Chen, Phonon conduction in PbSe, PbTe, and $PbTe_{1-x}Se_x$ from first-principles calculations, Phys. Rev. B **85**, 184303 (2012).

[61] D. Dangic, O. Hellman, S. Fahy, and I. Savic, The origin of the lattice thermal conductivity enhancement at the ferroelectric phase transition in GeTe, npj Comput. Mater. **7**, 57 (2021).

[62] M. Christensen, A. B. Abrahamsen, N. B. Christensen, F. Juranyi, N. H. Andersen, K. Lefmann, J. Andreasson, C. R. H. Bahl, and B. B. Iversen, Avoided crossing of rattler modes in thermoelectric materials, Nat. Mater. **7**, 811 (2008).

[63] W. Qiu, L. Xi, P. Wei, X. Ke, J. Yang, and W. Zhang, Part-crystalline part-liquid state and rattling-like thermal damping in materials with chemical-bond hierarchy, Proc. Natl. Acad. Sci. USA **111**, 15031 (2014).

[64] E. Di Lucente, M. Simoncelli, and N. Marzari, Crossover from Boltzmann to Wigner thermal transport in thermoelectric skutterudites, Phys. Rev. Res. **5**, 033125 (2023).

[65] A. Roy, Estimates of the thermal conductivity and the thermoelectric properties of $PbTiO_3$ from first principles, Phys. Rev. B **93**, 100101(R) (2016).

[66] J. S. Zhou and J. B. Goodenough, Unusual evolution of the magnetic interactions versus structural distortions in $RMnO_3$ perovskites, Phys. Rev. Lett. **96**, 247202 (2006).

[67] L.-D. Zhao, S.-H. Lo, Y. Zhang, H. Sun, G. Tan, C. Uher, C. Wolverton, V. P. Dravid, and M. G. Kanatzidis, Ultralow thermal conductivity and high thermoelectric figure of merit in SnSe crystals, Nature (London) **508**, 373 (2014).

[68] S. I. Kim, K. H. Lee, H. A. Mun, H. S. Kim, S. W. Hwang, J. W. Roh, D. J. Yang, W. H. Shin, X. S. Li, Y. H. Lee, G. J. Snyder, and S. W. Kim, Dense dislocation arrays embedded in grain boundaries for high-performance bulk thermoelectrics, Science **348**, 109 (2015).

[69] S. Ramawat, S. Kukreti, and A. Dixit, β-$SrZrS_3$: A superior intermediate temperature thermoelectric through complex band geometry and ultralow lattice thermal conductivity, Phys. Rev. Mater. **7**, 085403 (2023).

[70] M. Tachibana, T. Kolodiazhnyi, and E. Takayama-Muromachi, Thermal conductivity of perovskite ferroelectrics, Appl. Phys. Lett. **93**, 092902 (2008).

[71] T. Katsufuji, T. Saiki, S. Okubo, Y. Katayama, and K. Ueno, Thermal conductivity of $SrVO_3 - SrTiO_3$ thin films: Evidence of intrinsic thermal resistance at the interface between oxide layers, Phys. Rev. Mater. **2**, 051002(R) (2018).

[72] J. Ravichandran, A. K. Yadav, R. Cheaito, P. B. Rossen, A. Soukiassian, S. J. Suresha, J. C. Duda, B. M. Foley, C.-H. Lee, Y. Zhu, A. W. Lichtenberger, J. E. Moore, D. A. Muller, D. G. Schlom, P. E. Hopkins, A. Majumdar, R. Ramesh, and M. A. Zurbuchen, Crossover from incoherent to coherent phonon scattering in epitaxial oxide superlattices, Nat. Mater. **13**, 168 (2014).

[73] R. Venkatasubramanian, E. Siivola, T. Colpitts, and B. O'Quinn, Thin-film thermoelectric devices with high room-temperature figures of merit, Nature (London) **413**, 597 (2001).

[74] M. V. Simkin and G. D. Mahan, Minimum thermal conductivity of superlattices, Phys. Rev. Lett. **84**, 927 (2000).

[75] G. Chen, Thermal conductivity and ballistic-phonon transport in the cross-plane direction of superlattices, Phys. Rev. B **57**, 14958 (1998).

[76] E. A. Kraut, R. W. Grant, J. R. Waldrop, and S. P. Kowalczyk, Precise determination of the valence-band edge in x-ray photoemission spectra: Application to measurement of

semiconductor interface potentials, Phys. Rev. Lett. **44**, 1620 (1980).

[77] J. Euvrard, Y. F. Yan, and D. B. Mitzi, Electrical doping in halide perovskites, Nat. Rev. Mater. **6**, 531 (2021).

[78] J. Heyd, G. E. Scuseria, and M. Ernzerhof, Hybrid functionals based on a screened Coulomb potential, J. Chem. Phys. **118**, 8207 (2003).

[79] N. F. Hinsche, B. Y. Yavorsky, M. Gradhand, M. Czerner, M. Winkler, J. Konig, H. Bottner, I. Mertig, and P. Zahn, Thermoelectric transport in Bi_2Te_3/Sb_2Te_3 superlattices, Phys. Rev. B **86**, 085323 (2012).

[80] G. Tan, F. Shi, S. Hao, L.-D. Zhao, H. Chi, X. Zhang, C. Uher, C. Wolverton, V. P. Dravid, and M. G. Kanatzidis, Non-equilibrium processing leads to record high thermoelectric figure of merit in PbTe-SrTe, Nat. Commun. **7**, 12167 (2016).

[81] L.-D. Zhao, J. He, S. Hao, C.-I. Wu, T. P. Hogan, C. Wolverton, V. P. Dravid, and M. G. Kanatzidis, Raising the thermoelectric performance of p-type PbS with endotaxial nanostructuring and valence-band offset engineering using CdS and ZnS, J. Am. Chem. Soc. **134**, 16327 (2012).

[82] Z. Gao, X. Ning, J. Wang, J. Wang, and S. Wang, Ultrahigh power factor and ultralow thermal conductivity at room temperature in PbSe/SnSe superlattice: Role of quantum-well effect, Small **18**, 2104916 (2022).

[83] J. P. C. Baena, L. Steier, W. Tress, M. Saliba, S. Neutzner, T. Matsui, F. Giordano, T. J. Jacobsson, A. R. S. Kandada, S. M. Zakeeruddin, A. Petrozza, A. Abate, M. K. Nazeeruddin, M. Graetzel, and A. Hagfeldt, Highly efficient planar perovskite solar cells through band alignment engineering, Energy Environ. Sci. **8**, 2928 (2015).

[84] C.-H. M. Chuang, P. R. Brown, V. Bulovic, and M. G. Bawendi, Improved performance and stability in quantum dot solar cells through band alignment engineering, Nat. Mater. **13**, 796 (2014).

[85] A. Ishida, T. Yamada, D. Cao, Y. Inoue, M. Veis, and T. Kita, Seebeck effect in PbTe films and EuTe/PbTe superlattices, J. Appl. Phys. **106**, 023718 (2009).

[86] T. C. Harman, P. J. Taylor, D. L. Spears, and M. P. Walsh, Thermoelectric quantum-dot superlattices with high ZT, J. Electron. Mater. **29**, L1 (2000).

[87] J. P. Heremans, M. S. Dresselhaus, L. E. Bell, and D. T. Morelli, When thermoelectrics reached the nanoscale, Nat. Nanotechnol. **8**, 471 (2013).

[88] D. I. Bilc, G. Hautier, D. Waroquiers, G.-M. Rignanese, and P. Ghosez, Low-dimensional transport and large thermoelectric power factors in bulk semiconductors by band engineering of highly directional electronic states, Phys. Rev. Lett. **114**, 136601 (2015).

[89] Y. Pei, A. D. LaLonde, N. A. Heinz, X. Shi, S. Iwanaga, H. Wang, L. Chen, and G. J. Snyder, Stabilizing the optimal carrier concentration for high thermoelectric efficiency, Adv. Mater. **23**, 5674 (2011).

[90] Y. Pei, Z. M. Gibbs, A. Gloskovskii, B. Balke, W. G. Zeier, and G. J. Snyder, Optimum carrier concentration in n-type PbTe thermoelectrics, Adv. Energy Mater. **4**, 1400486 (2014).

[91] C. Liu, Z. Zhang, Y. Peng, F. Li, L. Miao, E. Nishibori, R. Chetty, X. Bai, R. Si, J. Gao, X. Wang, Y. Zhu, N. Wang, H. Wei, and T. Mori, Charge transfer engineering to achieve extraordinary power generation in GeTe-based thermoelectric materials, Sci. Adv. **9**, eadh0713 (2023).

[92] Z. Liu, W. Gao, H. Oshima, K. Nagase, C.-H. Lee, and T. Mori, Maximizing the performance of n-type Mg_3Bi_2 based materials for room-temperature power generation and thermoelectric cooling, Nat. Commun. **13**, 1120 (2022).

[93] A. P. Justl, F. Ricci, A. Pike, G. Cerretti, S. K. Bux, G. Hautier, and S. M. Kauzlarich, Unlocking the thermoelectric potential of the $Ca_{14}AlSb_{11}$ structure type, Sci. Adv. **8**, eabq3780 (2022).

[94] B. Jiang, W. Wang, S. Liu, Y. Wang, C. Wang, Y. Chen, L. Xie, M. Huang, and J. He, High figure-of-merit and power generation in high-entropy GeTe-based thermoelectrics, Science **377**, 208 (2022).

[95] C. Zhou, Y. K. Lee, Y. Yu, S. Byun, Z.-Z. Luo, H. Lee, B. Ge, Y.-L. Lee, X. Chen, J. Y. Lee, O. Cojocaru-Miredin, H. Chang, J. Im, S.-P. Cho, M. Wuttig, V. P. Dravid, M. G. Kanatzidis, and I. Chung, Polycrystalline SnSe with a thermoelectric figure of merit greater than the single crystal, Nat. Mater. **20**, 1378 (2021).

[96] Y.-K. Jung, I. T. Han, Y. C. Kim, and A. Walsh, Prediction of high thermoelectric performance in the low-dimensional metal halide $Cs_3Cu_2I_5$, npj Comput. Mater. **7**, 51 (2021).

[97] Z. Bu, X. Zhang, B. Shan, J. Tang, H. Liu, Z. Chen, S. Lin, W. Li, and Y. Pei, Realizing a 14% single-leg thermoelectric efficiency in GeTe alloys, Sci. Adv. **7**, eabf2738 (2021).

[98] Y. Wu, Z. Chen, P. Nan, F. Xiong, S. Lin, X. Zhang, Y. Chen, L. Chen, B. Ge, and Y. Pei, Lattice strain advances thermoelectrics, Joule **3**, 1276 (2019).

[99] G.-K. Ren, S. Wang, Z. Zhou, X. Li, J. Yang, W. Zhang, Y.-H. Lin, J. Yang, and C.-W. Nan, Complex electronic structure and compositing effect in high performance thermoelectric BiCuSeO, Nat. Commun. **10**, 2814 (2019).

[100] Q. Jin, S. Jiang, Y. Zhao, D. Wang, J. Qiu, D.-M. Tang, J. Tan, D.-M. Sun, P.-X. Hou, X.-Q. Chen, K. Tai, N. Gao, C. Liu, H.-M. Cheng, and X. Jiang, Flexible layer-structured Bi_2Te_3 thermoelectric on a carbon nanotube scaffold, Nat. Mater. **18**, 62 (2019).

[101] J. Li, X. Y. Zhang, Z. W. Chen, S. Q. Lin, W. Li, J. H. Shen, I. T. Witting, A. Faghaninia, Y. Chen, A. Jain, L. D. Chen, G. J. Snyder, and Y. Z. Pei, Low-symmetry rhombohedral GeTe thermoelectrics, Joule **2**, 976 (2018).

[102] S. Wang, J. Yang, L. Wu, P. Wei, J. Yang, W. Zhang, and Y. Grin, Anisotropic multicenter bonding and high thermoelectric performance in electron-poor CdSb, Chem. Mater. **27**, 1071 (2015).

[103] K. Biswas, J. He, I. D. Blum, C.-I. Wu, T. P. Hogan, D. N. Seidman, V. P. Dravid, and M. G. Kanatzidis, High-performance bulk thermoelectrics with all-scale hierarchical architectures, Nature (London) **489**, 414 (2012).

[104] X. Shi, J. Yang, J. R. Salvador, M. Chi, J. Y. Cho, H. Wang, S. Bai, J. Yang, W. Zhang, and L. Chen, Multiple-filled skutterudites: High thermoelectric figure of merit through separately optimizing electrical and thermal transports, J. Am. Chem. Soc. **133**, 7837 (2011).

[105] G. J. Snyder, M. Christensen, E. Nishibori, T. Caillat, and B. B. Iversen, Disordered zinc in Zn_4Sb_3 with phonon-glass and electron-crystal thermoelectric properties, Nat. Mater. **3**, 458 (2004).